Quantum state depression in metals and semiconductor quantum wells

Avtandil Tavkhelidze, Amiran Bibilashvili, Larissa Jangidze, Vasiko Svanidze
Javakhishvili Tbilisi State University, Chavchavadze Ave. 13, 0179 Tbilisi Georgia, avtotav@gmail.com

Abstract:
In this study, the quantum state depression (QSD) in metal films and semiconductor quantum well (QW) is investigated. The QSD emerge from the ridged geometry of the QW boundary. Ridges impose additional boundary conditions on the electron wave function and some quantum states become forbidden. State density reduces in all energy bands, including conduction band (CB). Hence, electrons, rejected from the filled bands, must occupy quantum states in the empty bands due to Pauli Exclusion principle. Both the electron concentration in CB and Fermi energy increases as in the case of donor doping. Since quantum state density is reduced, the ridged quantum well (RQW) exhibits quantum properties at widths of hundreds of nm. Wide RQW can be used to improve photon confinement in QW-based optoelectronics devices. Reduction in the state density increases the carrier mobility and makes the ballistic transport regime more pronounced in the semiconductor QW devices. Furthermore, the QSD doping does not introduce scattering centers and can be used for power electronics.

Keywords*: Quantum well, density of sates, optoelectronics, ballistic transport*

1. Introduction

Quantum well (QW) lasers, solar cells, and transistors are fabricated based on semiconductor heterostructure technologies.[1] Typical thickness of the QW layer is 10–20 nm. Lower thickness is essential to reduce the density of the quantum states and realize the quantum properties of the well. However, thin layers do not confine the photons (needed for optoelectronics) and do not carry high currents (needed for power electronics). Recently, quantum state depression (QSD) was investigated both theoretically[2] and experimentally.[3] The QSD allows reduction of quantum state density and realization of quantum properties of the thick layer. It is based on the ridged geometry of the layer boundary. Periodic ridges impose additional boundary conditions on the electron-wave function. Supplementary boundary conditions forbid some quantum states for free electrons, and the state density in **k** space $\rho(\mathbf{k})$ reduces. Due to the Pauli Exclusion principle, electrons rejected from the forbidden quantum states have to occupy the states with higher **k**. Thus, Fermi vector k_F and Fermi energy E_F increase. Under certain conditions an electron in a solid can be regarded as a planar wave. The main requirement that should be satisfied is that at least one dimension of the solid should be equal to or less than the mean free path of the electron inside the solid. In this case, the electron can move without scattering and could be regarded as de Broglie wave. It is difficult to satisfy this requirement in metals because the electron mean free path in metals is in the range of 1–5 nm at room temperature. Transport properties of metals (charge and heat transport) are defined by electrons having energies close to the Fermi level, and the mean free path is given for those electrons. Other free electrons, for instance, electrons having energies much below Fermi level in metals, do not participate in charge and heat transport, because it is quantum mechanically forbidden for them to exchange energy with the environment (all quantum energy levels nearby are occupied), and hence the mean free path of such electrons is formally infinite. Such electrons will remain ballistic inside relatively large metal structures.

We assume a solid with the surface geometry as shown in Fig. 1 (a) in which periodic indents are introduced in the flat surface of the solid. Let us consider an electron traveling towards the border of the solid as planar wave 1. Wave 1 will reflect back from the border of the solid because the electron
does not have enough energy to leave the solid. Because of the geometry of the surface there will be two reflected waves. One will reflect from the top of the indent (wave 3) and the other will reflect from the bottom of the indent (wave 2). If the indent depth is one quarter of the de Broglie wavelength of the electron, waves 2 and 3 will interfere destructively and there will be no reflected wave. As a result, an electron of certain energy cannot reflect back from the surface because of its wave nature. On the other hand, the electron cannot leave the solid and enter the vacuum because it does not have enough energy to overcome the potential barrier. Electron can not reflect under arbitrary angle since all quantum states in the Fermi gas are already occupied by other electrons. From the quantum mechanical point of view, we can say that all possible final quantum states for that particular electron are forbidden. Consequently, initial quantum state also becomes forbidden. As a result, the density of the quantum states inside the solid will be reduced. A three-dimensional (3D) drawing of the solid is shown in Fig. 1(b). If we regard the solid as a potential energy box, there will be standing de Broglie waves inside the solid. Each standing wave corresponds to the quantum state which could be occupied by the free electron. The number of standing waves inside such a 3D structure is lower than in the case in which there were no indents and all the walls of the solid were plain.

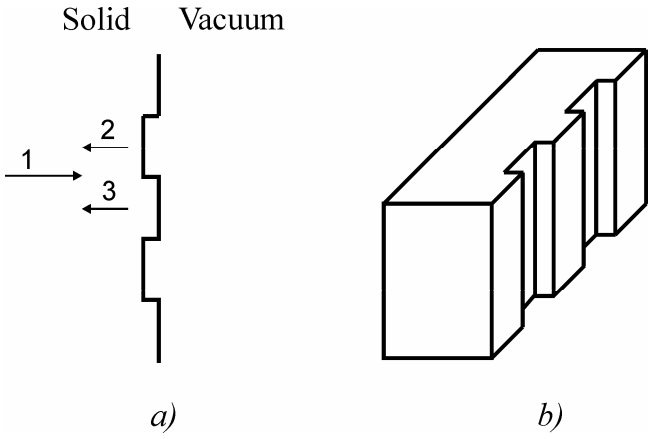

Fig. 1. (a) de Broglie wave interference diagram. (b) Geometry of modified potential energy box.

2. Experiment

Gold films, having indents on both sides, were prepared to observe the QSD effect (Fig. 2). Gold was the material of choice because it does not form natural oxide on the surface and allows exposure of the samples to the atmosphere. Au film was deposited on a Si/SiO_2 (dry thermal oxide) substrate, and, after a conventional cleaning procedure, a layer of photoresist S1813 of thickness of 0.4 um was attached at 4000 rpm (photoresist was solved prior to attachment). Optical microscope MII-4 was used for thickness control. Periodic lines 0.8 um wide were created in the photoresist using UV photolithography, and the SiO2 was etched using NH4F+HF+H2O, at a rate of 1 nm/ s to a depth of 10–50 nm. In the next step, the photoresist was removed using acetone followed by a conventional cleaning procedure. A further layer of photoresist was attached, and another photolithographic step was used to form large structures using a lift-off process. The substrate was then placed in a deposition chamber and, after a vacuum of 10−6 Torr was obtained, heated to 80°C to remove water from the surface.

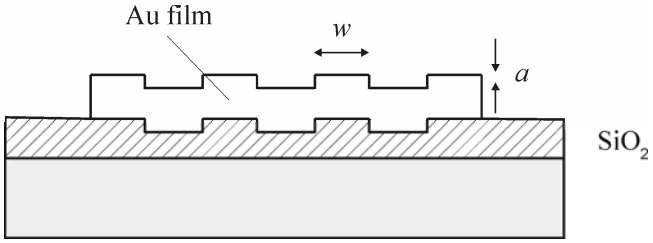

Fig. 2. Schematic cross sections of test samples. Adhesion layers between SiO2 and Au films are omitted for simplicity.

The substrate was cooled to temperatures between −16 and −22 °C, and a thin film of 2–3 nm thickness, evaporated from a mixture of Au and Cr, was deposited on SiO2 to form an adhesion layer (not shown in Fig. 2 for simplicity). Following deposition, the wafer was moved rapidly (maximum of 5 s) to another location, where a Au film of thickness of 60 nm was deposited using fast thermal evaporation of Au wire (99.999% purity). The substrate was heated up to room temperature and the wafer was taken out of the deposition chamber. The final step was a conventional lift-off process to form large structures.

Measurements of the work function were made using the Kelvin probe (KP) method. All measurements were comparative to exclude absolute inaccuracies: the difference between KP readings on a flat region of the gold film was compared with the reading from the indented region of the film. The structure of the films was analyzed using x-ray diffraction . For all samples measured, the indented regions showed a reduced work function (WF) compared with the flat regions. The magnitude of this reduction of WF depended on the structure of the gold film and the depth of the indents. Films having an amorphous structure show much higher reduction in WF than films having a polycrystalline structure. All polycrystalline films show a WF reduction less than 0.1 eV while for amorphous films the reduction of WF is in the range of 0.2–0.5 eV. Amorphous films were obtained by deposition of gold on cooled substrate (as described above), and polycrystalline ones were obtained by deposition of gold on room temperature substrate. No other technological parameter except substrate temperature was different in the two deposition processes. The difference in WF was more pronounced for samples that were deposited in a cleaner environment (by plasma cleaning the deposition chamber prior to deposition), since for the cooled wafer the residual gas pressure and composition have considerable influence on the structure of the film. The difference in WF reduction up to ten times shows that the structure of the film has principal importance for observation of the QSD effect. This experimental result is in full agreement with theory. One further unplanned experiment confirmed the importance of the structure of the film. When the Au film was fabricated in a deposition chamber previously used for Ca, it unexpectedly showed a reduction of WF of 0.06 eV instead of the expected 0.5 eV. Subsequent x-ray analysis revealed the presence of Ca atoms inside the Au film, and also the Au film was polycrystalline instead of amorphous. It was obvious that Ca contamination changed the film structure to polycrystalline, resulting in the QSD effect almost vanishing. After the deposition chamber was cleaned, new samples were fabricated which showed better amorphousness on x-ray analysis, and the WF difference increased to 0.2 eV. Fabrication of samples following further cleaning of the chamber, by dismantling followed by chemical and mechanical treatment to remove the thin layer of Ca completely from the parts of the deposition chamber, yielded Au films showing a WF reduction of 0.4 eV and having amorphous structure by x-ray analysis. It was observed that the strength of the effect depends on the depth of the indents. Samples having Au film thickness of 60 nm and indent depths of 50, 20, and 10 nm show WF reductions of 0.16, 0.25, and 0.56 eV, respectively. This experimental result is in quantitative agreement with the prediction of the theory.[2]

3. QSD in semiconductors

In semiconductors, QSD reduces $\rho(E)$ in all energy bands including the conduction band (CB). Electrons, rejected from the filled bands, occupy the quantum states in the empty bands, and the electron concentration in CB increases. This corresponds to donor doping. The QSD depends on electron confinement and, therefore, is most pronounced in QW structures.

Let us now find the distinctive features of the semiconductor RQW. Like in metals, the QSD also forbids some quantum states. However, before going into their details, the distinctions and similarities between the QSD forbidden state and a hole should be elucidated. The QSD forbidden state is forbidden by the boundary conditions and cannot be occupied. However, it is not forbidden in an irrevocable way. If the boundary conditions change (e.g., due to charge depletion), then the QSD forbidden state can recombine with the electron. As the QSD forbidden state is confined to the boundary conditions (macroscopic geometry), it is not localized in the lattice and cannot move like a hole.

The QSD transfers electrons to higher energy levels. If initially the semiconductor is of *p* type, then the QSD will change it to an undoped or even to *n* type. The QSD is comparable with a conventional donor doping, from the point of increase in E_F. However, there are no donor atoms in the case of QSD doping, which makes it akin to modulation doping. Unlike modulation doping, there is no space charge, as the QSD does not redistribute the charge and just transfers the electrons from the filled energy bands to the empty ones. Moreover, the material remains uniformly neutral.

It is convenient to make comparison between the RQW and QW. Furthermore, the main parameters, such as $\rho(\mathbf{k})$, $\rho(E)$, and E_F, of the RQW can be expressed in terms of the same parameters of conventional QW (a=0). It can be assumed that both the wells are made from the undoped material and are deep enough (to allow the limit of infinitely deep well). The $\rho(\mathbf{k})$ is inversely proportional to the volume of **k** space elementary cell. Cell volume for the RQW can be found [2] on the basis of volume perturbation method of solving the time-independent Schrödinger equation (Helmholtz equation).[4] However, this method can only be used when $a<<L_X$. The RQW volume is divided into two parts: main volume (MV) and additional volume (AV). It is presumed that MV>>AV and it defines the form of the solutions for the whole RQW volume. Subsequently, the solutions of the RQW volume are searched in the form of solutions of the MV. The method is especially effective in the case when MV has a simple geometry, e.g., rectangular geometry, allowing separation of the variables. In this study, the volume of the ridge was regarded as AV having dimensions a, w, L_z. The MV had the dimensions, L_x, L_y, L_z. Solutions were plane de Broglie waves with discrete k spectrum. Further, the electron-wave function and its derivative were matched from the two sides on the border of MV and AV. The result obtained was the reduction of $\rho(\mathbf{k})$ and the increase of E_F in RQW (detailed description can be found in Ref. 2). Analysis was made within the limit of the quantum model of free electrons. Here, we extrapolate the results to Bloch waves with the assumption that, the electron energy is $E(k)=\hbar^2k^2/2m^*$ and m^* is energy independent, where $\hbar$ is the Planks constant and m^* is an electron effective mass.

The k space elementary cell volumes for RQW and QW are $(2\pi)^3/awL_z$ and $(2\pi)^3/L_xL_yL_z$, respectively (as found in Ref. 2). Here, L_x, L_y, and L_z are the well dimensions. Thus, the corresponding (not normalized) state densities, $P(\mathbf{k})$ are

$$P_{\mathrm{RQW}}(\mathrm{k})=\frac{2awL_z}{(2\pi)^3},\quad P_{\mathrm{QW}}(\mathrm{k})=\frac{2L_xL_yL_z}{(2\pi)^3}\ . \tag{1}$$

Factor 2 accounts for the spin. Thus, the normalized state densities are

$$\rho_{\mathrm{RQW}}(\mathrm{k})=\frac{2}{(2\pi)^3}\frac{aw}{L_y(L_x+a/2)},\ \rho_{\mathrm{QW}}(\mathrm{k})=\frac{2}{(2\pi)^3}\ . \tag{2}$$

In Eq. (2), the real space volumes of RQW and QW are considered, and we introduced the geometry factor

$$G = L_y(L_x + a/2)/aw. \tag{3}$$

Thus, the comparison in Eq. (2) gives that $\rho_{\mathrm{RQW}}(\mathrm{k}) = \rho_{\mathrm{QW}}(\mathrm{k})/G$. State density in **k** is reduced by factor *G*. The periodic lattice potential does not depend on QSD, and hence, m^* and the dispersion relation $E(k)$ are identical for both RQW and QW. The state density in energy $\rho(E) = (dE/d\mathrm{k})^{-1}\rho(\mathrm{k})$ is reduced by the same factor *G*, i.e.,

$$\rho_{\mathrm{RQW}}(E) = \rho_{\mathrm{QW}}(E)/G. \tag{4}$$

Subsequently, the concentration of the QSD-generated electrons $\mathrm{n_{QSD}}$ was determined. The quantum well layer was typically grown on a substrate of diverse band structures. A general case shown in Fig. 3 demonstrates that the bandgaps of the substrate material are wider. The QSD takes place within the electron confinement intervals ΔE_j, where j=1, ..., 4. Each ΔE_j has the characteristic dispersion relation $E_\mathrm{j}(k) = \hbar^2k^2/2m_\mathrm{j}^*$ and density of states $\rho^{(\mathrm{j})}(E)$. Here, m_j^* is the electron effective mass within the *j*th interval. Inside each ΔE_j, there exist QSD forbidden states, whose densities are and Eq. (4) was used in Eq. (5).

$$\rho_{\mathrm{FOR}}^{(\mathrm{j})}(E) = \rho_{\mathrm{QW}}^{(\mathrm{j})}(E) - \rho_{\mathrm{RQW}}^{(\mathrm{j})}(E) = \rho_{\mathrm{QW}}^{(\mathrm{j})}(E)(1 - G^{-1}) \tag{5}$$

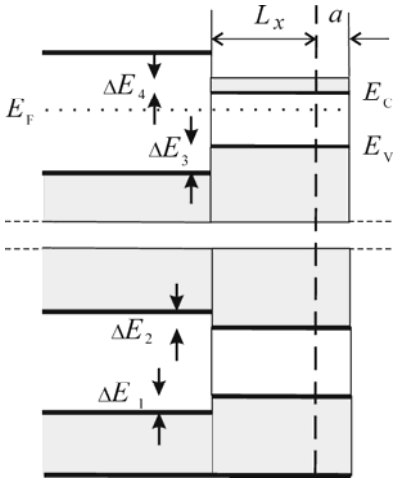

Fig. 3. Energy diagram of semiconductor RQW grown on wide bandgap substrate.

The total density of the forbidden states is the sum of the densities of the forbidden states from all intervals ΔE_j, i.e.,

$$\rho_{\mathrm{FOR}} = \sum_\mathrm{j} \rho_{\mathrm{FOR}}^{(\mathrm{j})}(E) = (1 - G^{-1}) \sum_\mathrm{j} \rho_{\mathrm{QW}}^{(\mathrm{j})}(E). \tag{6}$$

The sum $\sum_\mathrm{j} \rho_{\mathrm{QW}}^{(\mathrm{j})}(E)$ depends on the band structures of both the substrate and RQW material, and can be calculated for a particular pair. Apparently, the sum does not depend on the QSD. Thus, the expression $n_{\mathrm{CON}} \equiv \sum_\mathrm{j} \rho_{\mathrm{QW}}^{(\mathrm{j})}(E)$ is introduced, and the index shows that it is the electron confinement-defined number. The n_{CON} does not depend on the energy, since the summation by energy was already carried out. Thus, according to Eq. (6), the total number of forbidden quantum states (per unit volume) or concentration of QSD-generated electrons can be rewritten as

$$\mathrm{n_{QSD}} = \rho_{\mathrm{FOR}} = n_{\mathrm{CON}}(1 - G^{-1}) \ . \tag{7}$$

Equation (7) gives the QSD doping. To calculate other RQW parameters, we used the condition of electrical neutrality.[5]

$$\mathrm{n_{RQW}} = \mathrm{p_{RQW}} + \mathrm{n_{QSD}} = \mathrm{p_{RQW}} + n_{\mathrm{CON}}(1 - G^{-1}). \tag{8}$$

where n_{RQW} and p_{RQW} are the electron and hole concentrations in the RQW. They can be found using the semiconductor equation for the non-degenerate limit, as follows:

$$n_{RQW}p_{RQW} = \frac{N_C}{G}\frac{N_V}{G}\exp(-E_g / K_B T) = \frac{n_{QW}^2}{G^2} = n_i^2. \quad (9)$$

Here, N_C and N_V are the effective state densities in CB and VB of QW, $E_g=E_c-E_v$ is the bandgap width, K_B is Boltzmann's constant, T is the absolute temperature, n_{QW} is the electron concentration in QW, and n_i is the initial (to QSD doping) electron concentration in RQW. To obtain Eq. (9), we divided the state densities by a factor G according to Eq. (4), and used the semiconductor equation for the conventional QW $n_{QW}^2 = N_C N_V \exp(-E_g / K_B T)$. The combination of Eq. (8) and Eq. (9) gives

$$n_{RQW} = \frac{1}{2G}\left\langle n_{CON}(G-1) + \left[n_{CON}^2 (G-1)^2 + 4n_{QW}^2 \right]^{1/2} \right\rangle, \quad (10)$$

where n_{RQW} is similar to n_{QW} in the limits of QSD absence. The first limit is G=1 (no state density reduction). Equation (10) shows that for G=1, $n_{RQW} = n_{QW}$. Another limit is n_{CON}=0 (no confinement), in which Eq. (10) gives $n_{RQW} = n_{QW}/G$, where the latter is not similar to n_{QW} for any value of G. Divergence is apparent, since G can have only one value of G=1 in the case of zero confinement. Actually, n_{CON}=0 corresponds to no boundaries and no RQW geometry. The p_{RQW} can be obtained from Eq. (10) and Eq.(9).

Subsequently, we determined the increase in E_F due to QSD doping ΔE_F. We used the formula $\Delta E_F = k_B T \ln(n_{RQW} / n_i)$ for the non-degenerate limit.[5] By inserting n_{RQW} from Eq. (10) and n_i from Eq. (9), we get

$$\Delta E_F = k_B T \ln\left\langle \frac{n_{CON}(G-1)}{2n_{QW}} + \left[\frac{n_{CON}^2 (G-1)^2}{4n_{QW}^2} + 1 \right]^{1/2} \right\rangle. \quad (11)$$

Figure 4 demonstrates the ΔE_F dependence on n_{CON} for some values of G according to Eq. (11). The ΔE_F is most sensitive to changes in G for low G value ($G \approx 1$). For G>3, the dependence is less sensitive to changes in G and is linear in the logarithmic scale. Such behavior is natural, as for G with somewhat exceeding unity, the state density remains high and small increase in the value of G generates large number of QSD-rejected electrons. On the contrary, for $G>3$, the state density is reduced dramatically, and further increase of G, does not generate that much rejected electrons. In addition, the ΔE_F will further increase for $(n_{CON}/n_{QW})>10^5$. However, we do not extend the curves, since Eq. (11) is true only within the non-degenerate limit. In the case of higher n_{CON}/n_{QW} when the semiconductor becomes degenerated, Fermi integrals should be used to calculate the n_{RQW} and ΔE_F. However, this could be done only within the limited energy range near the bottom of CB, since the above analysis is true only in the approximation that m^* is energy independent.

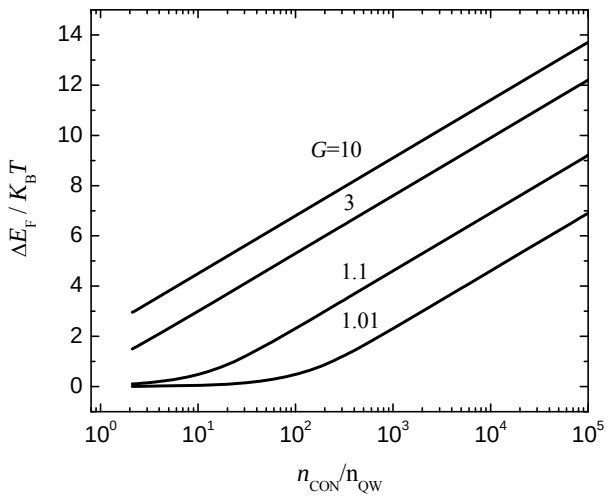

Fig. 4. Fermi energy increase as the function of QSD doping for some values of G.

Charge carrier scattering rates are proportional to $\rho(E)$ according to Fermi's golden rule and are reduced in RQW. If τ is the carrier transport lifetime, then according to Eq. (4), we have $\tau_{\mathrm{RQW}} = G\tau_{\mathrm{QW}}$. Consequently, for mobility $\mu = e\tau / m^*$, we get

$$\mu_{\mathrm{RQW}} = G\,\mu_{\mathrm{QW}} \ . \tag{12}$$

The mobility of charge carriers increases G times in the RQW. In the case of heavy QSD doping (n_{RQW}>>p_{RWQ}), the hole current can be neglected and the electrical conductivity using Eq. (12) in Eq. (13) is given as

$$\sigma_{\mathrm{RQW}} = e\,\mu_{\mathrm{RQW}}\,\mathrm{n}_{\mathrm{RQW}} = \sigma_{\mathrm{QW}}\,G\,(\mathrm{n}_{\mathrm{RQW}} / \mathrm{n}_{\mathrm{QW}}) . \tag{13}$$

Furthermore, by inserting Eq. (10) in Eq. (13), we get

$$\sigma_{\mathrm{RQW}} = \sigma_{\mathrm{QW}} \left\langle \frac{n_{\mathrm{CON}}(G-1)}{2\mathrm{n}_{\mathrm{QW}}} + \left[\frac{{n_{\mathrm{CON}}}^2 (G-1)^2}{4{\mathrm{n}_{\mathrm{QW}}}^2} + 1 \right]^{1/2} \right\rangle . \tag{14}$$

Equation (14) indicates that the conductivity of RQW increases with respect to QW. Figure 5 shows the conductivity dependence on QSD-generated electron concentration for some values of G. In the general case, the hole current contributes to the mechanism and should be included in Eq. (13), and can be calculated in a similar way using p_{RQW} determined from Eqs (10) and (9).

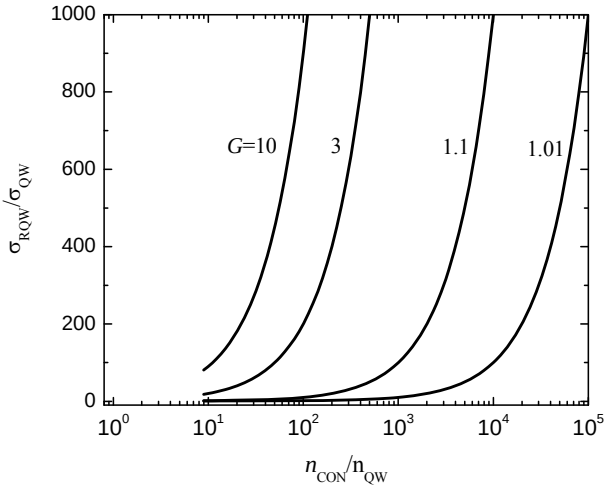

Fig.5. Conductivity dependence on QSD doping for some values of G.

4. Geometry Factor Calculation

Conventional QW (a=0) has quasi-2D structure L_y,L_z >> L_x and no quantum features are considered in the Y and Z directions. Non-normalized state density is $P(E) = \rho(E)\,L_x\,S$, where S is a layer surface, $P(E)$ is proportional to the product $\rho(E)L_x$. As $\rho(E)$ in RQW is reduced G times, L_x can be similarly increased with respect to G times without the loss of quantum properties. Let us find G for the arbitrary geometry. There are no analytical solutions to the time-independent Schrödinger equation in the ridged well (solution contains infinite sums). However, there are fairly accurate mathematical and numerical methods. Mathematically, there is no difference between QSD and electromagnetic mode depression, and Helmholtz equation and the same boundary conditions are used in both the cases. Helmholtz spectrum calculation can be found in the literature related to Casimir effect. Casimir energy exhibits strong dependence on photon spectrum and consequently, on the geometry of the vacuum gap.[6] A number of geometries, including double-side ridged geometry [7] were analyzed. In addition, a software designed for wave-mode calculation in ridged waveguides has been developed,[8, 9] and can be used to determine G numerically.

In practice, w>>a, which allows the assumption that k spectrum is quasi-continuous in Y direction. Thus, in the first approximation, G can be rewritten in a simpler form as

$$G = (L_x + a/2)/a \approx L_x / a \ . \tag{15}$$

In Eq. (15), we consider that $a<<2L_x$, which is satisfied automatically within the perturbation method limit [Eq. (3) is obtained using perturbation method]. We presume that this method is precise enough in the range of $5<(L_x/a)<10$, and Eq. (15) can be used for that range (the method cannot be used for $a \to 0$, since diffraction leads to ignoring the ridges by wave). Therefore, we used the values of $G= 5 \div 10$ for further estimations. In practice, 20-nm wide conventional QW can be replaced by $100 \div 200$-nm wide RQW.

5. Possible Applications

Condition for observation of quantum effects $E_{n+1} - E_n >> K_B T$ limits increase in RQW thickness. Energy difference between consecutive energy levels should be much more than thermal energy. For instance if QW of thickness of 20 nm exhibits quantum properties at T=300 K, then RQW made of same material will exhibit quantum properties at thickness of maximum Gx20 nm at T=300 K. Thickness could be increased further only in the case temperature is lowered. However this limitation applies only to energy levels which are close to Fermi energy (i.e at the top of VB and bottom of CB). Electrons having energies $E<<E_V$ do not interact with environment and consequently are not influenced by thermal fluctuations (Ref 3). Last means that QSD doping is practically not limited by thermal fluctuations.

5.1 QSD in solar cells and power electronics

For optoelectronics and power electronics it is important to have suitable wide bandgap materials. [10] Intrinsic semiconductors with E_g>1.5 eV are difficult to utilize as their electrical conductivity is very low. Doping is typically used to increase electron concentration in CB. However, conventional doping introduces impurity centers and increases electron scattering. QSD doping can be used to solve the problem. It increases electron concentration in CB without introducing scattering centers. Besides it, QSD reduces scattering rates in both CB and VB.

QW embedded in p-i-n junction is frequently used for solar cells. [11, 12] Typical QW layer is only 10-20 nm thick and there is the light confinement problem. To overcome it, complicated multiple QW heterostructures are fabricated. QSD can contribute in difficulty solving. Thicker RQW layer has the same quantum properties . This increases light confinement. Reduced number of RQW layers will be needed. Combination of QW and RQW can also be used for solar cells. Here we describe one

possible combination. Single QW is embedded inside the RQW (Fig. 6(a) shows energy diagram). For comparison, in the same figure we give energy diagram of QW, embedded inside the conventional QW (Fig. 6(b)). The QW in QW system has low $P(E)$ within the energy range $E_{C3} < E < E_{C2}$ (E_{C3}, E_{C2}, E_{C1} are CB bottoms).

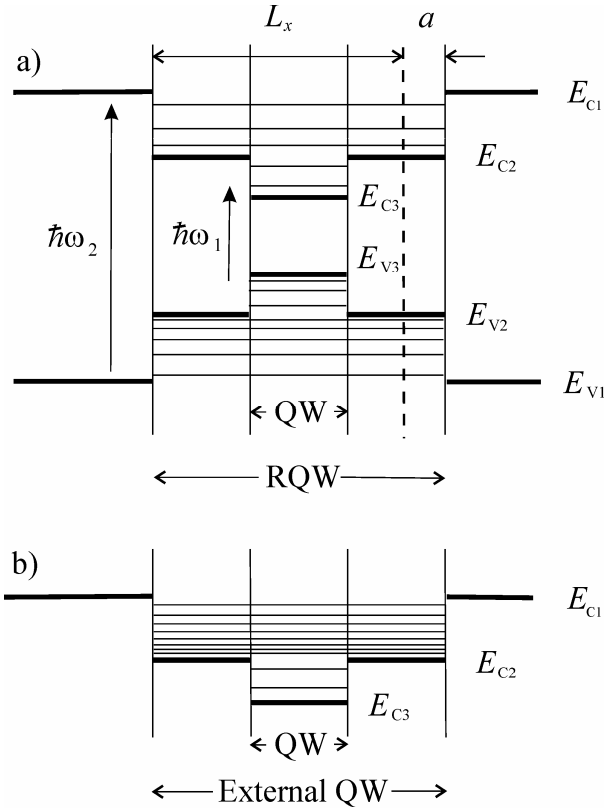

Fig.6 Energy diagrams for a) QW inside the RQW, b) QW inside the QW heterostructures. Horizontal lines depict energy levels. It is assumed that energy spectrum is continious above E_{C1} and below E_{V1}..

This is due to narrow internal QW. In the range $E_{C2} < E < E_{C1}$, $N(E)$ is higher as external QW is wider (Fig.4(b)). We replace external QW by the RQW of same width (Fig.6(a)). Then, $P(E)$ reduces due to QSD inside the energy range $E_{C2} < E < E_{C1}$. As result, we get system which has low $P(E)$ in broad energy range $E_{C3} < E < E_{C1}$ (same is true for holes in VB, Fig.6(a)). Parameter G can be selected so that, state densities match (Eq. (4)). Such RQW(QW) heterostructure has quantum properties close to the internal QW. Simultaneously it has same low $P(E)$ in broader energy range and is itself wider than internal QW. It has almost uniform $P(E)$ over energy range $E_{C3} < E < E_{C1}$. Consequently, broad photon spectrum $\omega_1 < \omega < \omega_2$ (ω is frequency of incident photon) can be efficiently converted into electricity as system exhibits quantum properties in broad energy range $\hbar\omega_1 < E < \hbar\omega_2$. This is important because in practical devices energy spectrum above E_{c1} and below E_{v1} is continuous and for $\omega > \omega_2$ energy conversion becomes inefficient. Furthermore, as QW embedded inside the RQW heterostructure is wider, it better confines light. It also has higher electrical conductivity due to low $P(E)$.

5.2 QSD laser with tunable wavelength

QW is often used for heterostructure lasers. [13, 14] Let us consider p-n-n^+ junction laser based on RQW. Fig. 7 shows energy diagram for RQW hetrostructure. RQW is embedded between p doped and n doped layers. n doped layer is subsequently n^+ doped to the depth, not approaching RQW from the right side, as shown in Fig 7. RQW is QSD-n doped. When current flows through p-n-n^+ junction, electrons and holes recombine inside the RQW. Photon with energy $\hbar\omega_0$, is emitted.

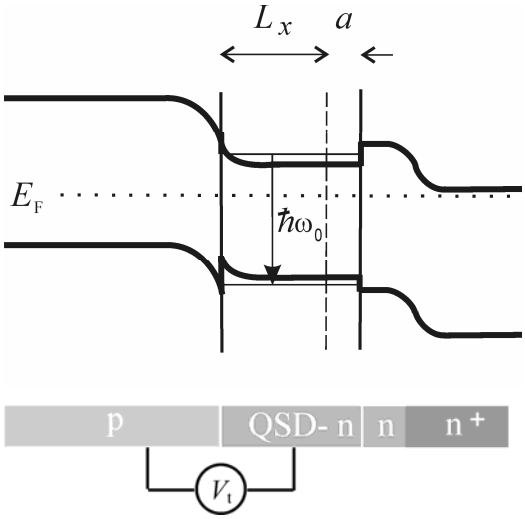

Fig. 7 Energy diagram of tunable RQW light emitting diode. Horisontal lines, in CB and VB of GaAs, depict energy levels.

Since RQW could be made as thick as 200 nm, it becomes possible to tune its width using charge depletion (depletion region width is typically more than 100 nm). Voltage V_t is applied to p-n junction. It modifiers internal potential and charge distribution in the proximity of RQW left boundary. Effective L_x of RQW changes and consequently G alters. G becomes V_t dependent and positions of energy levels (both in CB and VB) move on energy scale. Emitted photon energy $\hbar\omega_0$ is tuned. QSD doping of working area allows low resistive loses and high efficiency. Width of RQW can be maximized by choosing high G. At the same time QSD doping of working area can be regulated by adjusting n_{CON} (Eq. 10).

5.3 QSD effect MOS transistor

Ballistic MOSFET transistors are widely discussed in the literature. [14, 16, 17] Ballistic regime is difficult to realize in practice because it requires very thin channel. Using RQW in the transistor channel reduce $n(E)$ and consequently, channel thickness could be increased G times. One of the possible designs of QSD MOS transistor is shown in Fig. 8(a).

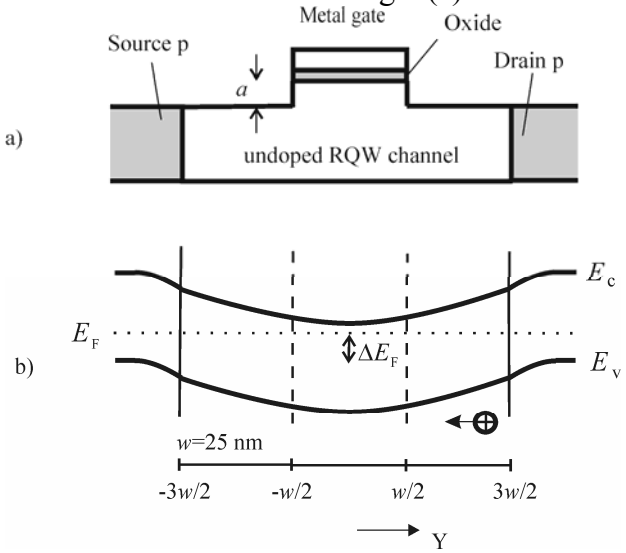

Fig. 8 a) p-i-p type QSD transistor, b) corresponding energy diagram.

Channel made from undoped material has a single ridge. Insulator layer and gate electrode are grown on the top of the ridge. QSD doping converts undoped channel to n-type under the ridge. Far from the ridge E_F remains unaffected, as there is no QSD influence. Energy diagram is shown on Fig. 8(b). There is a pocket for electrons in CB and a potential barrier for holes in VB. ΔE_F depends

on G and consequently on dimensions a, $L_{x.}$ Further, effective a can be altered by applying external voltage to the gate electrode and depleting charge under the insulator. ΔE_F changes according to Eq. (11). As result, gate voltage modulates current in source-drain channel. Above design corresponds to p type source and drain electrodes (p-i-p) transistor, since holes are charge carriers (barrier is in VB). If carriers are electrons (n-i-n transistor), barrier in CB is needed and different geometry should be used.

For description of channel electrostatic potential ϕ we used 1D Poisson equation basically following calculations made in ref 18.

$$\frac{\mathrm{d}^2\phi}{\mathrm{d}y^2} - \frac{\phi - V_g}{\lambda^2} = -\frac{4\pi}{\varepsilon_S}\rho(y) \tag{13}$$

Here, V_g is gate voltage, λ is effective screening length, ε_S is dielectric penetrability of channel. Using Eq. (11) we find QSD generated charge density as function of ΔE_F in the middle of channel (y=0)

$$\rho(0) = 2\,q\,n_{QW}\sinh(\Delta E_F / K_B T) \quad . \tag{14}$$

Here, q is electron charge. Further, we use bell curve $\exp(-\alpha y^2)$ to simulate distribution of QSD generated charge density $\rho(y) = \rho(0)\exp(-\alpha y^2)$. Coefficient α was determined from boundary condition: $\rho(3w/2) = \rho(-3w/2) = q(n_{QW}/10)$. Such boundary conditions follow from considering that, QSD generated electron concentration is much less than initial electron concentration at the channel boundaries (channel length is 3w). Next, we assume that doping level is high in source and drain electrodes. Consequently, QSD generated field is fully concentrated inside the channel. We used conventional formulas for MOS structure [5] to determine depletion depth under the gate electrode

$$d(V_g) = \left\langle \frac{2\varepsilon_S}{\rho(0)}\left[V_g + V_0 - (2V_0V_g + V_0^2)^{1/2}\right]\right\rangle^{1/2} . \tag{15}$$

Here, constant $V_0 = \left(\frac{\varepsilon_S}{\varepsilon_{OX}}\right)\frac{\rho(0)}{\varepsilon_{OX}}d_{OX}^2$, ε_{OX} is dielectric penetrability inside insulator layer and d_{OX} is oxide thickness. Effective ridge height was found as $a_{eff.}(V_g)=a-d(V_g)$. Fig. 9 shows potential distribution inside the channel for set of V_g. Following values were used: ΔE_F =0.3 eV, source-drain voltage V_{SD}=0, source-channel internal potential difference -0.3 V, w=25 nm, L_x=3 nm, a=1 nm, d_{ox} =2.5 nm, λ=6.8 nm, ε_{OX}=4, ε_S=12.

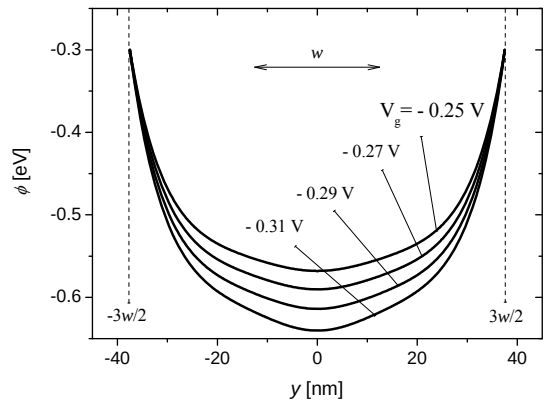

Fig. 9 Distribution of hole potential energy ϕ inside the channel for several gate voltages. λ=6.8 nm, w=25 nm, G=3, V_{SD}=0

For transistor I-V characteristics we found source-drain current as $J_{SD}=J_S-J_D$, where $J_{S,D} = q\,n_{S,D}(y)v_{S,D}(y)$. Here $v_{S,D}$ is charge carrier speed. Currents were calculated in the same way as in ref. 18. Resulting I-V characteristics are shown in Fig. 10. Above calculations are made

for p-i-p transistor. Thy can be extended to n-i-n. In last case potential will change sign and carrier effective mass will change.

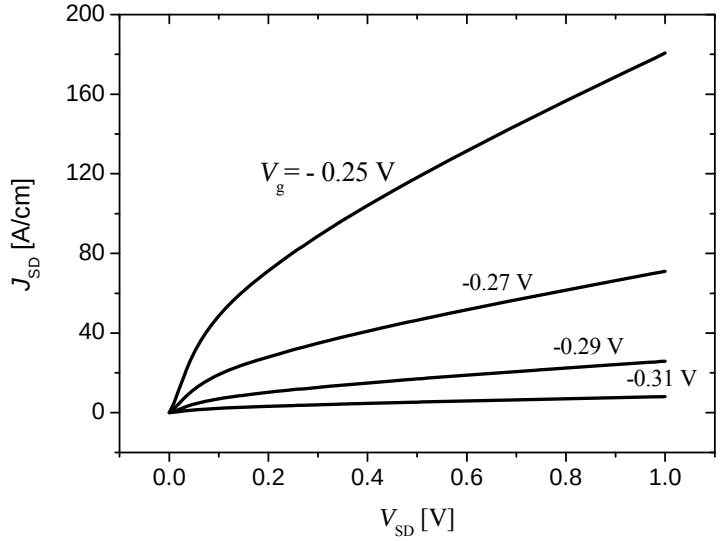

Fig. 10. I-V curves of p-MOS QSD transistor for several gate voltages.

One more advantage of transistor shown in Fig.8 is that current do not flow in close proximity of the semiconductor insulator junction. Junction is in the "bay" under the gate electrode. Such arrangement reduces insulator influence on hole mobility (through insulator impurities and surface roughness). [19]

QSD can also be used in diffusion transport MOS transistors, bipolar transistors and diodes. Combination of QSD doping with conventional and modulation doping will enable number of new designs.

5.4 RQW fabrication technology

MBE is typically used to grow quantum well layers. RQW growth do not differs from a conventional QW growth, except RQW layer has more thickness. It can become simpler to fabricate from the point of view of thickness accuracy. Ridges could be fabricated using e-beam lithography followed by ion etching or wet etching. RQW is thicker than QW and technological problems introduced by layer thickness become solvable (for instance, relative thickness of natural oxide, developed during lithography, becomes negligible for RQW). Native oxide can be removed usind annealing in situ . [20, 21] Since RQW is hundreds of nanometers thick, different fabrication methods can also be used. Namely, silicon on insulator (SOI) technology can be utilized to cleave and bond layers of that thickness. [22] SOI allows mechanical attachment of RQW layer to the substrate, instead of growing it using complicated MBE technology. Universal intermediate transfer wafer can be used to attach RQW layers one by one (Fig. 10). After oxidation and Hydrogen implantation Si wafer is bonded to transfer wafer.[23] Transfer wafer has etched vias for the purpose of future debonding. Next, ion-cut process is used to split Si wafer. Afterwards Si layer is polished and bonded to heterustructure surface.

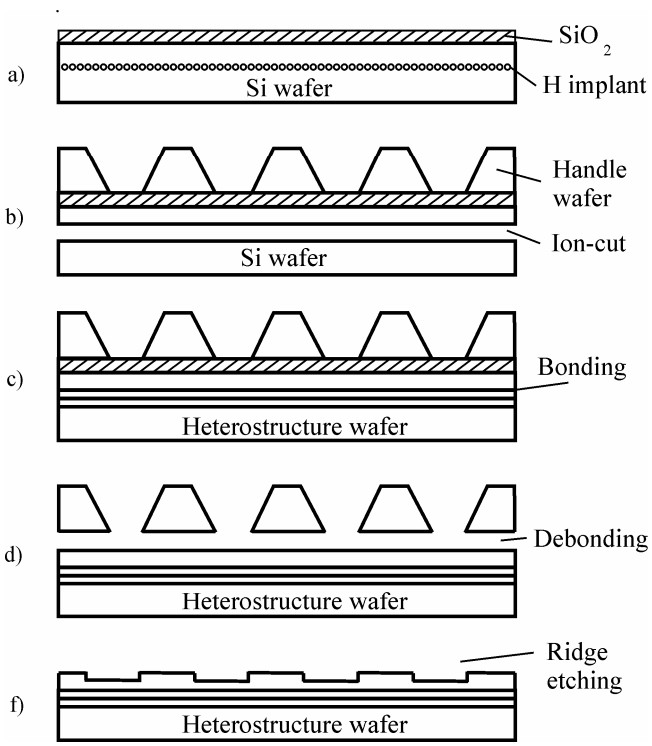

Fig. 10 RQW heterostructure fabrication by SOI technology and intermediate transfer wafer. a) Oxidation of Si wafer surface followed by Hydrogen inplantation. b) SiO_2 bonding to intermediate transfer wafer (having etched vias) followed by ion-cut splitting and polishing. c) Bonding to heterostructure. d) Etching SiO_2 and debonding transfer wafer. f) Etching ridges.

Final step is debonding of transfer layer by the way of etching Si oxide through the vias. Subsequently, ridges can be fabricated using conventional lithography. Process can be repeated to attach next RQW, using universal transfer layer Furthermore, in many cases (devices shown on figures 6, 8), ridged layer is the last epitaxial one. This allows conventional methods of ridge fabrication both for of SOI and MBE grown layers.

6. Conclusions

QSD in semiconductor ridged quantum well was studied. It was shown that QSD reduces the density of quantum states by geometry factor *G*. Electrons from the filled energy bands are transferred to CB. Since electron concentration in CB increase, QSD corresponds to donor doping. Like modulation doping, QSD doping does not introduce the impurities. QSD increase charge carrier mean free path $\approx G$ times. Formulas for carrier concentrations and E_F were obtained in non-degenerate limit. The RQW parameters were expressed in terms of conventional QW parameters.

RQW exhibits the same quantum properties as a QW at *G* times more width. This can be used in application such as power electronics, solar cells, semiconductor lasers, and MOS transistors. For power electronics, QSD can increase electron concentration in CB, without introducing scattering centers. For solar cells, using combination of RQW and QW can widen the converted light waveband, and increase efficiency. For lasers, RQW can allow tuning of emitted light wavelength. For MOS transistors, RWQ increase channel width and reduce influence of insulator layer.

Acknowledgments

Authors thank R. Melkadze for useful discussions. Work is partly supported by Borealis Technical Limited, assignee of corresponding U.S. patents (7,220,984; 7,166,786; 7,074,498; 6,281,514; 6,495,843; 6,680,214; 6,531,703; and 6,117,344).

References:

1. J.H. Davies, *The physics of low-dimensional semiconductors*, (Cambridge university press, 1998).
2. A. Tavkhelidze, V. Svanidze, and I. Noselidze, Fermi gas energetics in low-dimensional metals of special geometry, J. Vac. Sci. Technol. B, **25** (2007) 1270; Avto Tavkhelidze and Vasiko Svanidze, Quantum state depression in semiconductor quantum well, International Journal of Nanoscience, v. 7, No. 6, pp. 333-338, (2008).
3. A. Tavkhelidze, A. Bibilashvili, L. Jangidze, A. Shimkunas, P. Mauger, G.F. Rempfer, L. Almaraz, T. Dixon, M.E. Kordesch, N. Katan, and H. Walitzki, Observation of quantum interference effect in solids, J. Vac. Sci. Technol. B, **24** (2006) 1413.
4. V. M. Sedykh, *Waveguides With Cross Section of Complicated Shape* (Kharkhov University Press Kharkov, 1979), p. 16.
5. S. M. Sze, *Physics of semiconductor devices*, (Willey-Interscience publication, 2007).
6. Thorsten Emig, Andreas Hanke, Ramin Golestanian and Mehran Kardar, Probing the Strong Boundary Shape Dependence of the Casimir Force**,** Phys.Rev.Lett. **87**, (2001) 260402.
7. Rauno Büscher and Thorsten Emig, Geometry and Spectrum of Casimir Forces**,** Phys. Rev. Lett. **94**, (2005) 133901.
8. FIMMMWAVE, photon design software (A fully vectorial 2D Mode Solver), http://www.photond.com/products/fimmwave.htm.
9. CONCERTO, software for electromagnetic design, Vector Fields, http://www.vectorfields.com.
10. Wataru Saito, Yoshiharu Takada, Masahiko Kuraguchi, Kunio Tsuda, Ichiro Omura and Tsuneo Ogura, Design and Demonstration of High Breakdown Voltage GaN High Electron Mobility Transistor (HEMT) Using Field Plate Structure for Power Electronics Applications, Jpn. J. Appl. Phys. **43** (2004) pp. 2239-2242 .
11. J. C. Rimada , L. Hernández, J. P. Connolly and K. W. J. Barnham, Conversion efficiency enhancement of AlGaAs quantum well solar cells, Microelectronics Journal**, 38** (2007) pp. 513-518.
12. D. B. Bushnell, T. N. D. Tibbits, K. W. J. Barnham, J. P. Connolly, M. Mazzer, N. J. Ekins-Daukes, J. S. Roberts, G. Hill, and R. Airey, Effect of well number on the performance of quantum-well solar cells, J. Appl. Phys., **97** (2005) 124908 .
13. Kuniyoshi Okamoto, Hiroaki Ohta, Shigefusa F. Chichibu, Jun Ichihara, and Hidemi Takasu, Continuous-Wave Operation of *m*-Plane InGaN Multiple Quantum Well Laser Diodes, Jpn. J. Appl. Phys. **46** (2007) pp. L187-L189.
14. Seong-Ju Bae, Seoung-Hwan Park and Yong-Tak Lee, Bandgap Effects of Quantum Well Active-Layer on Threshold Current Density, Differential Gain and Temperature Characteristics of 1.3 μm InGaAlAs/InP Quantum Well Lasers, Jpn. J. Appl. Phys. 41 (2002) pp. 1354-1358.
15. Shanbhag, K.R. and Subramaniam, P.C. , Quantum Modeling of Nanoscale MOSFET, in: Physics of Semiconductor Devices, 2007. IWPSD 2007. International Workshop on, (2007) pp. 257-260.
16. M. H. Liao and C. W. Liu, Gate width dependence on backscattering characteristics in the nanoscale strained complementary metal-oxide-semiconductor field-effect transistor, Appl. Phys. Lett. **92** (2008) 063506.
17. K. K. Likharev, in: J. Greer *et al.* (eds.), *Nano and Giga Challenges in Microelectronics* (Elsevier, Amsterdam, 2003), p 27.
18. F. G. Pikus and K. K. Likharev, Nanoscale field-effect transistors: An ultimate size analysis, Appl. Phys. Lett. **71** (1997), pp.3661-3663.
19. T. Khan, D. Vasileska, and T. J. Thornton, Effect of interface roughness on silicon-on-insulator–metal-semiconductor field-effect transistor mobility and the device low-power high-frequency operation, J. Vac. Sci. Technol. B, 23 (2005) 1782.
20. Tatsuya Ogawa, Hiroaki Morota and Sadao Adachi, Thermal annealing behaviours of GaP(001) surface J. Phys. D: Appl. Phys. **40,** 4603–4609 (2007).
21. Jiro Osaka, Koichi Maezawa, Haruki Yokoyama andMasafumi Yamamoto, Highly Uniform Regrown $In_{0.53}Ga_{0.47}As$/AlAs/InAs Resonant Tunneling Diodes on $In_{0.53}Ga_{0.47}As$, Jpn. J. Appl. Phys. **38** (1999) pp. 1204-1207
22. O. Moutanabbir, B. Terreault, N. Desrosiers, A. Giguère, G. G. Ross, M. Chicoine, and F. Schiettekatte, Hydrogen Cleaving of Silicon at the Sub-100-nm Scale, *AIP Conf. Proc*. 772, 1491 (2005).
23. C. Colinge, B. Roberds and B. Doyle, Silicon Layer Transfer Using Wafer Bonding and Debonding , Journal of ELECTRONIC MATERIALS, **30**, No7, (2001), p. 841,

Article received: 2009-03-21